A Modified Directional Flame Thermometer: Development, Calibration, and Uncertainty Quantification

J. M. Cabrera
Department of Mechanical Engineering,
The University of Texas at Austin,
Austin, TX 78712
e-mail: janmichael.cabrera@mail.utexas.com

R. D. Moser
Institute for Computational
Engineering and Sciences,
The University of Texas at Austin,
Austin, TX 78712
e-mail: rmoser@ices.utexas.edu

O. A. Ezekoye[1]
Department of Mechanical Engineering,
The University of Texas at Austin,
Austin, TX 78712
e-mail: dezekoye@mail.utexas.edu

The directional flame thermometer (DFT) is a robust device used to measure heat fluxes in harsh environments such as fire scenarios but is large when compared to other standard heat flux measurement devices. To better understand the uncertainties associated with heat flux measurements in these environments, a Bayesian framework is utilized to propagate uncertainties of both known and unknown parameters describing the thermal model of a modified, smaller DFT. Construction of the modified DFT is described along with a derivation of the thermal model used to predict the incident heat flux to its sensing surface. Parameters of the model are calibrated to data collected using a Schmidt–Boelter (SB) gauge with an accuracy of ±3% at incident heat fluxes of 5 kW/m^2, 10 kW/m^2, and 15 kW/m^2. Markov Chain Monte Carlo simulations were used to obtain posterior distributions for the free parameters of the thermal model as well as the modeling uncertainty. The parameter calibration process produced values for the free parameters that were similar to those presented in the literature with relative uncertainties at 5 kW/m^2, 10 kW/m^2, and 15 kW/m^2 of 17%, 9%, and 7%, respectively. The derived model produced root-mean-squared errors between the prediction and SB gauge output of 0.37, 0.77, and 1.13 kW/m^2 for the 5, 10, and 15 kW/m^2 cases, respectively, compared to 0.53, 1.12, and 1.66 kW/m^2 for the energy storage method (ESM) described in ASTM E3057. [DOI: 10.1115/1.4046657]

1 Introduction

Measuring the heat flux is often important to the experimentalist seeking to characterize thermal–physical systems. To the fire scientist, doing so accurately is a difficult task because most sensors either do not take into account all the relevant physical effects or are not robust enough to withstand the severe environments of compartment fires. There are commercially available sensors that can be used to measure heat fluxes such as Gardon and Schmidt–Boelter (SB) gauges. These sensors require liquid cooling that can cause condensation on the sensor surface, are generally calibrated with radiative heat transfer thus creating large errors when other modes of heat transfer are important, are generally quite expensive, and also not suitable to the environments a fire scientist is interested in where high heat fluxes or soot deposition can either damage or foul the sensor.

Development of robust heat flux sensors for the fire environment has been a long sought after goal with early mentions of such devices being developed in the United Kingdom [1]. Sandia National Laboratories (SNL) has also developed a ruggedized heat flux gauge (HFG) consisting of an insulation packed, hollow cylinder with sensing plates at either ends. Blanchet et al. describe the construction, modeling considerations, and develop an uncertainty model given a step response to the sensor [2]. The model that is developed for the device uses finite difference methods to determine the temperature distributions within the sensing plates and insulation, and it is compared against measurements taken with a Gardon gauge. They note that the uncertainty can be a function of many components including the flux level, rate of change of flux level, time, and heating history. Victor Figueroa and cowokers also conduct an uncertainty analysis for the same device, using an inverse heat transfer code [3]. They report uncertainties of between 15% and 19% at high heat fluxes noting that the model is most sensitive to uncertainties in temperature histories, plate thicknesses, and the volumetric heat capacity of the sensing plates.

Blanchat and Hanks contrast multiple heat flux gauges (Gardon, Schmidt–Boelter, directional flame thermometer (DFT), and a high temperature heat flux sensor) exposed to a stair step exposure using a six-panel cylindrical array of high-temperature tungsten lamps [4]. They note overall good agreement between the sensors for flux conditions ranging between 100 kW/m^2 and 1000 kW/m^2. Bryant et al. present the uncertainty analysis of an SB gauge exposed to a radiative flux noting uncertainties as low as 6% for fluxes near flashover conditions [5]. Lam and Weckman expose four heat flux sensors (Gardon, SB, DFT, and HFG) to differing radiative and convective conditions using the heating element from an ASTM E1354 cone calorimeter and the hot flow from a heat gun [6]. They note comparable performance of the DFT to the SB and Gardon gauges to within 12% with the highest differences occurring during forced convective conditions.

Nakos performs an analysis of heat fluxes measured from a hydrocarbon fuel fire using three heat flux measurement techniques reporting large uncertainties in the measurements due to the mixed heat transfer mechanisms taking place [7]. Erikson et al. use finite difference methods and computational fluid dynamics to analyze uncertainties in a typical DFT and HFG with a heat source provided by aluminized solid propellant [8]. They note high uncertainties when using a compuational fluid dynamics code to model the heat transfer to the sensors.

ASTM E3057, Standard Test Method for Measuring Heat Flux Using Directional Flame Thermometers with Advanced Data Analysis Techniques has recently been introduced outlining the construction and data analysis of a typical DFT, reiterating much of the uncertainty results presented above [9]. Accurately quantifying the uncertainty for DFTs is a difficult task that is heavily dependent on the experimental conditions and modeling assumptions for the heat transfer coefficient. Propagation of uncertainty is

---

[1] Corresponding author.

Manuscript received November 15, 2019; final manuscript received February 24, 2020; published online March 30, 2020. Assoc. Editor: Kyle Daun.

an important aspect when the sensor measurements are used to inform fire models.

In the literature presented, standard statistical methods are used to propagate uncertainties of known parameters through the models describing the DFT. They also generally rely on reported values for the physical parameters to make approximations to the heat fluxes measured. Because the models are rigidly defined, it is not possible for DFT measurements to approach the predictive power of the more accurate gauges. The typical DFT also only provides an approximation to the local incident heat flux. Because of its size, the DFT measures a spatially averaged heat flux over its surface, increasing the uncertainty in the measurement.

In this work, we describe the construction of a smaller DFT, and derive a thermal model similar to those presented in Blanchet et al. and the energy storage method (ESM) presented in ASTM E3057 [2,9]. We allow some parameters within the model to vary and calibrate these parameters to measurements made using an SB gauge in a controlled environment to improve the predictive power of the model. Recently, there has been a resurgence in Bayesian methods for uncertainty quantification due to the increase in computational power that makes performing Markov chain Monte Carlo (MCMC) simulations tractable. We use this Bayesian framework to quantify the uncertainty of the SB gauge as well as to propagate uncertainties of known and unknown parameters through the model.

2 The Modified Directional Flame Thermometer

The typical DFT is constructed using two oxidized Inconel or stainless steel plates each instrumented with thermocouples. The plates sandwich, usually compressing slightly, ceramic fiber insulation at a known, fixed distance using stainless steel fasteners and spacers.

Our first attempts to modify the DFT consisted merely of reducing the size approximately 40% from the usual 120.65 mm × 120.65 mm (4.75 in. × 4.75 in.) square plates to 76.2 mm × 76.2 mm (3.0 in. × 3.0 in.), leaving the spacers and fasteners the same as a typical DFT. It was noticed, however, that conduction losses from the top plate through the bolts were greater than anticipated necessitating the use of smaller fasteners and low conductivity spacers. The resultant DFT is thus constructed of 76.2 mm × 76.2 mm × 1.6 mm thick (3.0 in. × 3.0 in. × 0.0625 in. thick), instrumented and coated stainless steel plates, sandwiching ceramic fiber insulation, and held together with 19 mm (0.75 in.) tall rigid ceramic fiber spacers and stainless steel fasteners. The emissivity of the coating used varied less than 5% between room temperature and 600 K when tested using a FLIR E40 IR camera [10].

3 Forward Model

It is relatively easy to calibrate and obtain measurements from heat flux gauges such as the Gardon gauge and SB gauge whose voltage response is linear with incident heat flux. Directional flame thermometers, while robust and simple in construction, require a much more in-depth analysis of the recorded data. This is a result of attempting to infer the heat flux to the device given the time–temperature history of the two metal plates using a thermo-physical model. Section 3.1 describes derivation of this model in detail.

3.1 Thermo-Physical Model.

3.1 Thermo-Physical Model. When the DFT is placed with one of its two metal plates facing a heat source, that plate will increase in temperature and heat transfer through the device will ensue. Analysis of this heat transfer process is what allows one to determine the incident heat flux to the device. The analysis is fundamentally determined by the models used for heat transfer to the device, heat transfer within the device, and the thermo-physical parameters of these models.

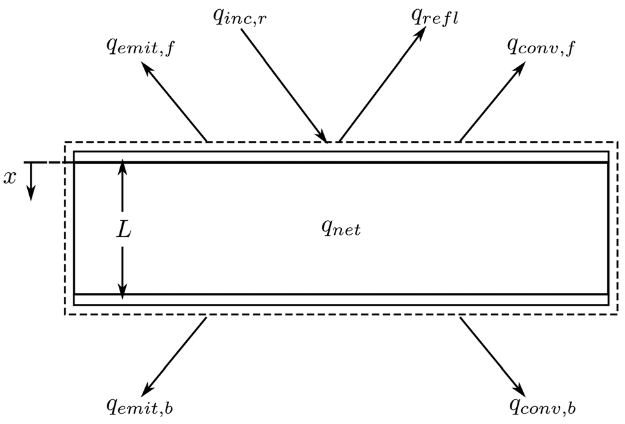

Fig. 1 Energy balance on a typical DFT

3.1.1 Heat Transfer Mechanisms. Figure 1 shows a typical DFT and its corresponding control volume exposed to some incident heat flux as well as the associated losses from the DFT. Applying an energy balance with no energy generation to the control volume, we obtain for the total rate of energy stored per unit area within the system[2]

$$q_{\mathrm{st,tot}} = q_{\mathrm{inc},r} - q_{\mathrm{refl}} - q_{\mathrm{emit},f} - q_{\mathrm{conv},f} - q_{\mathrm{emit},b} - q_{\mathrm{conv},b} \quad (1)$$

where $q_{\mathrm{inc},r}$ is the incident radiative heat flux on the front plate, q_{refl} is the component of the incident heat flux that is reflected from the front plate of the DFT, $q_{\mathrm{emit},f}$ and $q_{\mathrm{emit},b}$ are the emitted heat fluxes by the front and back plates of the DFT as it increases in temperature and exchanges energy with its surroundings. The convective losses (natural or forced) from the front and back plates to the surrounding fluid are denoted by $q_{\mathrm{conv},f}$ and $q_{\mathrm{conv},b}$, respectively. The reflected heat flux, q_{refl} can be written as

$$q_{\mathrm{refl}} = (1-\alpha)q_{\mathrm{inc},r} \quad (2)$$

where α is the absorptivity of the plate surface.

Simple models are employed for the radiative and convective heat transfer mechanisms from the front and back surfaces of the DFT. The emitted fluxes are thus

$$q_{\mathrm{emit},f} = \varepsilon\sigma(T_f^4 - T_{\mathrm{sur}}^4); \qquad q_{\mathrm{emit},b} = \varepsilon\sigma(T_b^4 - T_{\mathrm{sur}}^4) \quad (3)$$

where T_f, T_b, and T_{sur} are the front plate temperature, back plate temperature, and temperature of the surroundings far from the DFT, respectively. The emissivity of the plates are denoted by ε and σ is the Stefan–Boltzmann constant. Similarly, the convective losses from the front and back surfaces of the DFT are modeled using Newton's law of cooling

$$q_{\mathrm{conv},f} = h_f(T_f - T_\infty); \qquad q_{\mathrm{conv},b} = h_b(T_b - T_\infty) \quad (4)$$

with T_f, T_b, and T_∞ being the front plate temperature, back plate temperature, and temperature of the fluid far from the DFT, respectively. The heat transfer coefficients for the front and back plates are h_f and h_b, respectively, and for natural convection are parameterized by

$$h = \frac{\mathrm{Nu}\cdot k_{\mathrm{air}}}{L_{\mathrm{ch}}}; \quad \mathrm{Nu} = C\cdot \mathrm{Ra}^n; \quad \mathrm{Ra} = \frac{g\beta_{\mathrm{air}}(T-T_\infty)L_{\mathrm{ch}}^3}{\nu_{\mathrm{air}}\alpha_{\mathrm{air}}} \quad (5)$$

Combining Eqs. (2)–(4) with Eq. (1), and solving for the incident heat flux assuming $\alpha \approx \varepsilon$ as is done in ASTM E3057 [9], one obtains

---

[2] Here we have chosen to drop the conventional use of the double prime to indicate a flux value.

$$q_{\mathrm{inc},r} = (q_{\mathrm{st,tot}}/\varepsilon) + \sigma(T_f^4 - T_{\mathrm{sur}}^4) + \sigma(T_b^4 - T_{\mathrm{sur}}^4) + h_f/\varepsilon(T_f - T_\infty) + h_b/\varepsilon(T_b - T_\infty) \tag{6}$$

ASTM E3057 describes a number of methods with which to model the energy stored $q_{\mathrm{st,tot}}$ [9]. We will be utilizing and calibrating our own heat transfer model and later compare the results to the ESM described in ASTM E3057.

3.1.2 *One-Dimensional Conduction.*

For the model presented here, the rate of total energy per unit area stored within the DFT is the sum of the rate of energy stored in the front plate, $q_{\mathrm{st},f}$, the back plate, $q_{\mathrm{st},b}$, and the insulation, $q_{\mathrm{st,ins}}$

$$q_{\mathrm{st,tot}} = q_{\mathrm{st},f} + q_{\mathrm{st},b} + q_{\mathrm{st,ins}} \tag{7}$$

With an effective radiative heat transfer coefficient of the order 10 W/m^2 K ($h_r \equiv \varepsilon(T_s + T_{\mathrm{rad}})(T_s^2 + T_{\mathrm{rad}}^2)$) typical of environments where a DFT would be deployed, a characteristic plate thickness of order 10^{-3} m and representative thermal conductivity of order 10 W/m K, the Biot number can be shown to be much less than one. The energy storage terms for the front and back plates assuming they are thermally lumped are then

$$q_{\mathrm{st},f} = \rho_s c_{p,s} l_s \frac{dT_f}{dt}; \qquad q_{\mathrm{st},b} = \rho_s c_{p,s} l_s \frac{dT_b}{dt} \tag{8}$$

where ρ_s and $c_{p,s}$ are the density and specific heat of the plates, respectively. The rate of energy stored per unit area in the front and back plates of the DFT can be solved for given the time–temperature history for each plate.

The one-dimensional (1D), transient heat conduction equation with constant thermal conductivity is used to solve the temperature distribution within the insulation

$$\frac{\partial T_{\mathrm{ins}}}{\partial t} = \alpha_{\mathrm{ins}} \frac{\partial^2 T_{\mathrm{ins}}}{\partial x^2} \tag{9}$$

where α_{ins} is the thermal diffusivity of the insulation. The boundary conditions for the insulation are $T(x=0,t) = T_f$ and $T(x=L,t) = T_b$, and the initial condition is $T(x,t=0) = T_0$.

With the spatial-temporal temperature distribution within the insulation calculated, the energy flows into and out of the insulation are solved for using Fourier's law of conduction

$$q_{\mathrm{in,ins}} = -k_{\mathrm{ins}} \left.\frac{dT_{\mathrm{ins}}}{dx}\right|_{x=0}; \qquad q_{\mathrm{out,ins}} = -k_{\mathrm{ins}} \left.\frac{dT_{\mathrm{ins}}}{dx}\right|_{x=L} \tag{10}$$

Applying energy conservation to only the insulation one can obtain the rate of energy stored per unit area as the energy flowing into the insulation minus that leaving it

$$q_{\mathrm{st,ins}} = q_{\mathrm{in,ins}} - q_{\mathrm{out,ins}} \tag{11}$$

3.1.3 *Energy Storage Method.*

The ESM described in ASTM E3057 aims to solve a simplified form of the energy equation derived in Sec. 3.1.2. The net heat flux is claimed to be the energy stored in the front plate of the DFT, the energy stored in the insulation, and the energy lost through the insulation to the back plate

$$q_{\mathrm{net,esm}} = \left(\rho_s c_{p,s} l_s \frac{dT_{\mathrm{DFT}}}{dt}\right) + \left(k_{\mathrm{ins}} \frac{T_f - T_b}{L_{\mathrm{ins}}}\right) + \left(\rho_{\mathrm{ins}} c_{p,\mathrm{ins}} L_{\mathrm{ins}} \frac{dT_{\mathrm{ins,esm}}}{dt}\right) \tag{12}$$

The first term on the right-hand-side of Eq. (12) is the energy stored within the front plate with $T_{\mathrm{DFT}} = T_f$. The second term corresponds to the energy conducted through the insulation. The last term approximates the energy stored within the insulation with $T_{\mathrm{ins,esm}} \approx (T_f + T_b)/2$. The steel density, specific heat, and thickness are ρ_s, $c_{p,s}$, and l_s, respectively. The insulation density, specific heat, and thickness are ρ_{ins}, $c_{p,\mathrm{ins}}$, and L_{ins}, respectively. Given the time–temperature history of the front and back plates, Eq. (12) is readily solved for.

3.2 Thermo-Physical Properties.

It is necessary to define thermo-physical parameters to bring closure to the models presented in Secs. 3.1.2 and 3.1.3. Many of the properties are easily measured such as the plate and insulation thicknesses, and others yet are commonly available in the literature (i.e., thermal conductivity, density, etc.). For calibration purposes, however, it is required that some subset of the parameters that define the model be free to vary. We choose to vary parameters that are both uncertain and that which the model is sensitive to. To perform this analysis, the first-order sensitivity coefficients of the model are estimated. The total variance of heat flux measurement associated with the model parameters assuming only first-order interactions where each W_j is estimated as a first-order Taylor-series expansion is

$$W = \sum_{j=1}^{J} W_j; \quad W_j = \left(\frac{\partial q_{\mathrm{inc},r}}{\partial \Theta_j} \delta\Theta_j,\right)^2 \tag{13}$$

where $\Theta = \{\varepsilon, k_{\mathrm{ins}}, \rho_s c_{p,s}, l_s, L, C, n\}$. The first-order sensitivity coefficients are then

$$S_j = \frac{W_j}{W} \tag{14}$$

Table 1 shows the partial derivatives of the 1D conduction model in relation to components of the model, the variance for calculating the sensitivity coefficients [1], and the average sensitivity coefficient for a typical response evaluated at nominal parameter values. Perturbation was used to approximate the derivatives of parameters whose partial derivatives were analytically intractable.

A correlation for the volumetric heat capacity $\rho_s c_{p,s}$ of the plates was derived from data taken from Frank et al. [11]. Similarly, correlations were developed for the volumetric heat capacity and the thermal conductivity of the insulation with data taken from Keltner et al. [12], presented in Table 2. The plate thicknesses and insulation thickness were measured, and the standard deviation was estimated. Conservative estimates were imposed on

Table 1 Model parameter sensitivity coefficients

$\dfrac{\partial q_{\mathrm{inc},r}}{\partial \Theta_j}$	$\delta\Theta_j$	$\bar{S}_j$
$\dfrac{\partial q_{\mathrm{inc},r}}{\partial \varepsilon} = -\varepsilon^{-2}[q_{\mathrm{net}} + q_{\mathrm{conv}}]$	$\varepsilon \cdot 10\%$	0.659
$\dfrac{\partial q_{\mathrm{inc},r}}{\partial k_{\mathrm{ins}}} = \dfrac{1}{k_{\mathrm{ins}}\varepsilon}[q_{\mathrm{st,ins}}]$	$k_{\mathrm{ins}} \cdot 25\%$	0.062
$\dfrac{\partial q_{\mathrm{inc},r}}{\partial \rho_s c_{p,\mathrm{sf}}} = \dfrac{1}{\varepsilon \rho_s c_{p,\mathrm{sf}}}[q_{\mathrm{st},f}]$	$\rho_s c_{p,\mathrm{sf}} \cdot 5\%$	0.104
$\dfrac{\partial q_{\mathrm{inc},r}}{\partial \rho_s c_{p,\mathrm{sb}}} = \dfrac{1}{\varepsilon \rho_s c_{p,\mathrm{sb}}}[q_{\mathrm{st},b}]$	$\rho_s c_{p,\mathrm{sb}} \cdot 5\%$	0.008
$\dfrac{\partial q_{\mathrm{inc},r}}{\partial l_s} = \dfrac{1}{\varepsilon l_s}[q_{\mathrm{st},f} + q_{\mathrm{st},b}]$	$l_s \cdot 5\%$	0.117
$\dfrac{\partial q_{\mathrm{inc},r}}{\partial L} \approx \dfrac{q_{\mathrm{net}}(L) - q_{\mathrm{net}}(L + \delta L)}{\delta L}$	$L \cdot 5\%$	0.001
$\dfrac{\partial q_{\mathrm{inc},r}}{\partial C} = \dfrac{1}{\varepsilon C}[q_{\mathrm{conv}}]$	$C \cdot 10\%$	0.050
$\dfrac{\partial q_{\mathrm{inc},r}}{\partial n} = \dfrac{n}{\varepsilon \mathrm{Ra}_f} q_{\mathrm{conv},f} + \dfrac{n}{\varepsilon \mathrm{Ra}_b} q_{\mathrm{conv},b}$	$n \cdot 10\%$	0.000

Table 2 Curve fits to various thermo-physical properties

Property	Equation
Steel volumetric Heat capacity (J/m^3 K)	$\rho_s c_{p,s} = 5.54 \times 10^{-9}T^5 - 2.67 \times 10^{-5}T^4 + 4.98 \times 10^{-2}T^3 \cdots$ $-44.7T^2 + 2.04 \times 10^4 T + 5.13 \times 10^5$
Ceramic fiber volumetric Heat capacity (J/m^3 K)	$\rho_{\text{ins}} c_{p,\text{ins}} = -9.58 \times 10^{-8}T^4 + 3.31 \times 10^{-4}T^3 - 4.39 \times 10^{-1}T^2 \cdots$ $+3.21 \times 10^2 T + 8.15 \times 10^4$
Ceramic fiber thermal Conductivity (W/m K)	$k_{\text{ins}} = 7.36 \times 10^{-17}T^5 - 3.02 \times 10^{-13}T^4 4.87 \times 10^{-10}T^3 \cdots$ $-2.35 \times 10^{-7}T^2 + 1.43 \times 10^{-4}T + 3.11 \times 10^{-3}$

the uncertainty of C and n with nominal values taken as 0.54 and 0.25, respectively [11].

Of the model parameters presented in Table 1, it makes the most physical sense to allow ε, C, and/or n to vary as calibration parameters. The sensitivity analysis showed that the model is most sensitive to the emissivity, ε and correlation constant, C of the three parameters. We therefore use these parameters as candidates for the parameter calibration process. Section 4 outlines the experimental procedure used to calibrate the model with these parameters.

4 Experimental Setup

The DFTs were calibrated against a Schmidt–Boelter gauge that is accurate to within $\pm 3\%$ of the reading as specified by the manufacturer provided calibration certificate. The radiant element in an ASTM E1354 cone calorimeter was used to produce the necessary incident heat flux on both the SB gauge and the DFT [13]. A temporary fixture was installed on the side of the cone calorimeter to hold the DFT beneath the heating element. The stand that is normally used to measure the mass loss of specimens being tested to ASTM E1354 was temporarily removed to minimize the effects of reflected radiative heat transfer from surrounding objects. Figure 2 shows the DFT beneath the heating element.

Nakos and Engerer show that adjusting the sampling time of the DFT such that the Fourier number is greater than 0.5 will reduce the likelihood of noise being introduced into the data when using the ESM [1]. This threshold was used to determine a data sampling period of 0.5 s for all tests. To test the SB gauge it was placed with its top surface 25 mm from the bottom of the heating element. Tests were completed at three incident heat fluxes: 5 kW/m^2, 10 kW/m^2, and 15 kW/m^2. For each set-point the heating element was allowed to stabilize for a minimum of 15 min. Each test with the SB gauge consisted of 1 min of pretest data with the SB gauge unexposed to the heating element, 5 min exposed to the incident heat flux, and another minute unexposed to the heat flux. Three tests were completed at each of the set points with data taken using a Graphtec GL840 midi logger sampled at a period of 0.5 s.

Fig. 2 DFT being tested using an ASTM E1354 cone calorimeter heating element

Data recorded for the DFTs followed a similar procedure to that of the SB gauge. A total of 20 DFTs were tested at the same three incident heat fluxes: 5 kW/m^2, 10 kW/m^2, and 15 kW/m^2. The SB gauge was used to determine the set point of the heating element and was allowed to stabilize for 15 min after which it was removed to allow testing of the DFTs. The temperature data collected for each DFT followed the same procedure as above: 1 min of pretest, 5 min exposed to the incident heat flux, and 1 min of post-test sampled at a period of 0.5 s with a Graphtec GL840 midi logger.

With the calibration and DFT data, the thermo-physical model could be calibrated. Section 5 introduces the statistical framework used to process the data and to calibrate the parameters of interest for the model.

5 Statistical Framework

There are a number of ways to analyze observed data and calibrate models. Quantifying the uncertainty between model predictions and the observed data is also an important part of the calibration process. This is especially true for models that are intended to measure the environmental conditions that will further inform more complicated models.

Recently there has been a shift from orthodox, frequentist statistical methods to utilizing a Bayesian framework for inference and parameter calibration. The Bayesian framework is derived from a set of axioms, the Cox axioms, that consist of a simple set of consistency rules [14].

We choose to use this Bayesian framework to analyze the statistical models outlined in Secs. 5.1 and 5.2 to quantify the uncertainty in the calibration standard, calibrate the parameters of the model, and subsequently to quantify the total uncertainty of the calibration process. This framework most accurately represents the uncertainty in our parameters of interest; providing the best estimate for distributions on our parameters of interest (posterior probabilities) given our observations (likelihood) and prior information (prior probabilities). Bayes' rule can be summarized as

$$P(\theta|D) = P(\theta)\frac{P(D|\theta)}{P(D)} \tag{15}$$

where the posterior, $P(\theta|D)$ is the informed or "updated" distribution of the prior, $P(\theta)$, given observations, $P(D|\theta)$. The term in the denominator is known as the marginal likelihood, $P(D)$ and is usually ignored since it is required that the posterior probability be a proper probability distribution whose integral is unity across its support.

To close Eq. (15) prior distribution for $P(\theta)$ needs to be defined. This closure problem is a common one in Bayesian statistics with attempts made to create a completely objective way to perform inference. Here we choose to use Berger's method of objective

Bayes whose roots extend from efforts by Laplace, Jeffreys, and Jaynes [15–18]. This involves using proper priors where applicable and using conjugate improper, uninformative priors where we lack information to make the math tractable. Throughout, we use conventions described in *Joint Committee for Guides in Metrology (JCGM) 100:2008 Evaluation of measurement data—Guide to the expression of uncertainty in measurement* to describe random uncertainty as type A, and calibration uncertainties as type B [19].

The Bayesian framework is first used to quantify the uncertainty associated with the SB gauge measurements that will inform the model. Subsequently, the framework is used to consolidate the temperature data into a generative model that also has the consequence of smoothing fluctuations in the temperature data. Further, the framework is utilized to obtain posterior distributions for the quantities of interest, C and ε, as well as to quantify the uncertainty in the DFT measurements.

Throughout, index i refers to a single data point from a test set containing $I = 840$ total data points (7 min of data sampled at a period of 0.5 s). Index l refers to a particular test campaign: 5, 10, 15 kW/m^2 with a total of $L = 3$ campaigns. Index k refers to a particular replicate within a test campaign. For the SB gauge tests $K = 3$. For the DFT tests $K = 20$.

5.1 Data Reduction. Section 5.1.1 outlines the statistical framework used to summarize the data sets for the SB gauge and the DFTs. Simple Gaussian error models are used and MCMC techniques are used to obtain the relevant posterior distributions for parameters where applicable.

5.1.1 Schmidt–Boelter Gauge. It is assumed that any one data point, $q_{ikl}^{(\mathrm{inc},r)}$ is independent and identically distributed for the SB gauge. Given this, the statistical model is

$$q_{ikl}^{(\mathrm{inc},r)} = \bar{q}_{il}^{(\mathrm{inc},r)} + e; \quad e \sim N(0, \sigma_{\mathrm{sb},A}^2) \tag{16}$$

This suggests that for any replicate k, the true value is generated by some unknown heat flux $\bar{q}_{il}^{(\mathrm{inc},r)}$ plus mean zero Gaussian noise with variance $\sigma_{\mathrm{sb},A}^2$. The dataset across replicates for a single test campaign can be denoted by $D_{il} = \{q_{i1l}^{(\mathrm{inc},r)}, \ldots, q_{iKl}^{(\mathrm{inc},r)}\}$ where $K = 3$ for the SB gauge data. With these data, the likelihood is

$$P\left(D_{il} | \bar{q}_{il}^{(\mathrm{inc},r)}, \sigma_{\mathrm{sb},A}^2\right) = \left(\frac{1}{2\pi\sigma_{\mathrm{sb},A}^2}\right)^{K/2} \exp\left[-\frac{1}{2\sigma_{\mathrm{sb},A}^2}\sum_{k=1}^{K}\left(q_{ikl}^{(\mathrm{inc},r)} - \bar{q}_{il}^{(\mathrm{inc},r)}\right)^2\right] \tag{17}$$

Bayes' rule is used to find the posterior for $\bar{q}_{il}^{(\mathrm{inc},r)}$ given the likelihood

$$P(\bar{q}_{il}^{(\mathrm{inc},r)} | D_{il}, \sigma_{\mathrm{sb},A}^2) \propto P(\bar{q}_{il}^{(\mathrm{inc},r)}) P(D_{il} | \bar{q}_{il}^{(\mathrm{inc},r)}, \sigma_{\mathrm{sb},A}^2) \tag{18}$$

where the marginal likelihood, $P(D_{il})$ is ignored. The conjugate improper, uninformative prior (Jeffrey's prior) for a location parameter is $P(\bar{q}_{il}^{(\mathrm{inc},r)}) \propto 1$. The resulting posterior distribution $P(\bar{q}_{il}^{(\mathrm{inc},r)} | D_{il}, \sigma_{\mathrm{sb},A}^2)$ is Gaussian

$$\bar{q}_{il}^{(\mathrm{inc},r)} | D_{il}, \sigma^2 \sim N\left(\frac{1}{K}\sum_{k=1}^{K} q_{ikl}^{(\mathrm{inc},r)}, \sigma_{\mathrm{sb},A}^2\right) \tag{19}$$

This distribution states that at any time point i for campaign l the heat flux can be estimated as the arithmetic mean of the heat flux measurements taken across the $K = 3$ replicates.

Given the statistical model in Eq. (16), inference for the scaling parameter, $\sigma_{\mathrm{sb},A}^2$ requires the use of all the data across all replicates and campaigns. The resulting likelihood takes the form of

$$P\left(D | \bar{q}_{il}^{(\mathrm{inc},r)}, \sigma_{\mathrm{sb},A}^2\right) = \left(\frac{1}{2\pi\sigma_{\mathrm{sb},A}^2}\right)^{\mathrm{IKL}/2} \exp\left[-\frac{1}{2\sigma_{\mathrm{sb},A}^2}\sum_{ikl}\left(q_{ikl}^{(\mathrm{inc},r)} - \bar{q}_{il}^{(\mathrm{inc},r)}\right)^2\right] \tag{20}$$

where the triple product/sum is left implicit for brevity. Bayes' rule for the scaling parameter takes the form

$$P(\sigma_{\mathrm{sb},A}^2 | D, \bar{q}_{il}^{(\mathrm{inc},r)}) \propto P(\sigma_{\mathrm{sb},A}^2) P(D | \bar{q}_{il}^{(\mathrm{inc},r)}, \sigma_{\mathrm{sb},A}^2) \tag{21}$$

The Jeffrey's prior for a scaling parameter takes the form $P(\sigma_{\mathrm{sb},A}^2) \propto 1/\sigma_{\mathrm{sb},A}^2$ resulting in the inverse-Gamma posterior distribution for $\sigma_{\mathrm{sb},A}^2$ given the data

$$\sigma_{\mathrm{sb},A}^2 | D, \bar{q}_{il}^{(\mathrm{inc},r)} \sim \mathrm{IG}\left(\frac{\mathrm{IKL}}{2}, \frac{1}{2}\sum_{ikl}\left(q_{ikl}^{(\mathrm{inc},r)} - \bar{q}_{il}^{(\mathrm{inc},r)}\right)^2\right) \tag{22}$$

A Gibb's sampler as described in many modern statistics texts is used to reconstruct the conditional posterior distributions given by Eqs. (19) and (22) [20]. The resultant estimator for the scaling parameter is the mean of this distribution, presented here as the standard deviation: $\sigma_{\mathrm{sb},A} = 0.12$ kW/m^2. This result, however does not take into account type B (calibration) uncertainty. It has been shown that the total effect including this uncertainty for the heat flux measurement is [21]

$$\sigma_{\mathrm{sb,tot}}^2 = \sigma_{\mathrm{sb},A}^2 + \sigma_{\mathrm{sb},B}^2 \tag{23}$$

where $\sigma_{\mathrm{sb},B}$ is the type B uncertainty. We use $\sigma_{\mathrm{sb},B} = \pm 3\%$ of the measured value as stated by the manufacturer for this uncertainty.

5.1.2 Directional Flame Thermometer Temperatures. We seek to smooth the noisy temperature measurements generated by the data acquisition process when calibrating the 1D conduction model. Simply using the mean of the temperature samples will underestimate the true noise and therefore uncertainty present in the system. However, experience with the data acquisition system shows that periodically unrealistic jumps in the gradients of the temperatures taken will occur. Parametric, such as polynomial curve fitting and nonparametric regression such as Gaussian Process regression to the temperatures measured can have negative effects on the temporal gradients (a bias-variance tradeoff), greatly exaggerating the time response of the DFT [22]. As an alternative, a generative statistical model is developed that is informed by the data taken.

Let T_{kl} be a vector of temperature measurements from either the front or back surface of the DFT with length I from campaign l. It is assumed that the data generating process takes the following form:

$$T_{kl} = \bar{T}_l + e_l; \quad e_l \sim MVN(0, \Sigma_l) \tag{24}$$

where $\bar{T}_l$ is some unknown mean temperature for campaign l producing the observed data. Because the temperatures within a single measurement, T_{kl}, are highly correlated, the error term e_l is assumed to be a mean zero multivariate normal distribution in $\mathbb{R}^I$ with covariance Σ_l. While temperatures within a single dataset are assumed to be highly correlated, temperatures across data sets are assumed to be independent and identically distributed. Letting $D_l = \{T_{1l}, \ldots, T_{Kl}\}$, the likelihood for a single campaign for the front or back temperatures on the DFT becomes

$$P(D_l | \bar{T}_l, \Sigma_l) = \left(\frac{1}{(2\pi)^I |\Sigma_l|}\right)^{K/2} \times \exp\left[-\frac{1}{2}\sum_{k=1}^{K}(T_{kl} - \bar{T}_l)^{\mathrm{T}} \Sigma_l^{-1} (T_{kl} - \bar{T}_l)\right] \tag{25}$$

where $K = 20$ for the DFT experimental runs for a single campaign.

The joint posterior distribution for inferring $\bar{T}_l$ and Σ_l given the likelihood in Eq. (25) by Bayes' rule is defined as

$$P(\bar{T}_l, \Sigma_l | D_l) \propto P(\bar{T}_l, \Sigma_l) P(D_l | \bar{T}_l, \Sigma_l) \tag{26}$$

where again the marginal likelihood, D_l is dropped. Sun and Berger summarize the objective Bayesian methodology as applied to multivariate normal distributions [23]. We choose to use the Geisser and Cornfield improper, uninformative conjugate prior because it is frequentist matching for all means and variances [24]

$$P(\bar{T}_l, \Sigma_l) \propto |\Sigma_l|^{-I} \tag{27}$$

The posterior distribution for the mean, temperature, and the covariance for a given campaign then take the forms of a multivariate normal distribution and an inverse-Wishart distribution

$$\bar{T}_l | D_l, \Sigma_l \sim MVN\left(\frac{1}{K}\sum_{k=1}^{K} T_{kl}, \Sigma_l\right) \tag{28}$$

$$\Sigma_l | D, \bar{T}_l \sim W^{-1}\left(I + K, \Sigma_l^{-1} \sum_{k=1}^{K} (T_{kl} - \bar{T}_l)(T_{kl} - \bar{T}_l)^T\right) \tag{29}$$

where a Gibbs sampler was used to sample from the inverse-Wishart posterior. Figure 3 shows temperature measurements for the front and back plates of the DFTs at 5 kW/m^2, 10 kW/m^2 and 15 kW/m^2 in the left hand column for the 20 DFTs, and samples from the multivariate normal distributions parameterized by Eq. (28) in the right column. Solid lines and dashed lines represent the mean front and back plate temperatures for a test campaign, respectively.

Qualitatively, samples from the multivariate normal distributions appear to capture the temperature evolution well. Figure 3(*d*) also shows tempering of the temperature fluctuations as evaluated using the model while preserving average fluctuation amplitude. These sampled temperatures are what will be used to calibrate the model using the Bayesian approach outlined in Sec. 5.2.2.

5.2 Parameter Calibration. Calibration of the thermophysical model begins with finding the maximum likelihood estimate for our parameters of interest, $\hat{\theta}$ where $\hat{\theta} = \{\hat{C}, \hat{\varepsilon}\}$. This estimate is then used to inform the starting location for MCMC chains used to reconstruct the full probability distribution for of the parameters.

5.2.1 Maximum Likelihood. As before, we begin by defining the statistical model that generates the observed heat fluxes

$$\bar{q}_{il}^{(\mathrm{inc},r)} = \hat{\bar{q}}_{il}^{(\mathrm{inc},r)} + e_q; \qquad e_q \sim N(0, \sigma^2_{\mathrm{DFT},A}) \tag{30}$$

where $\bar{q}_{il}^{(\mathrm{inc},r)}$ is the mean heat flux measured by the SB gauge at some time index, i for campaign l. The heat flux predicted by the 1D conduction model using the mean front and back temperatures, $\bar{T}_{l,f}$ and $\bar{T}_{l,b}$ and with the parameters of interest, θ is $\hat{\bar{q}}_{il}^{(\mathrm{inc},r)}$. The

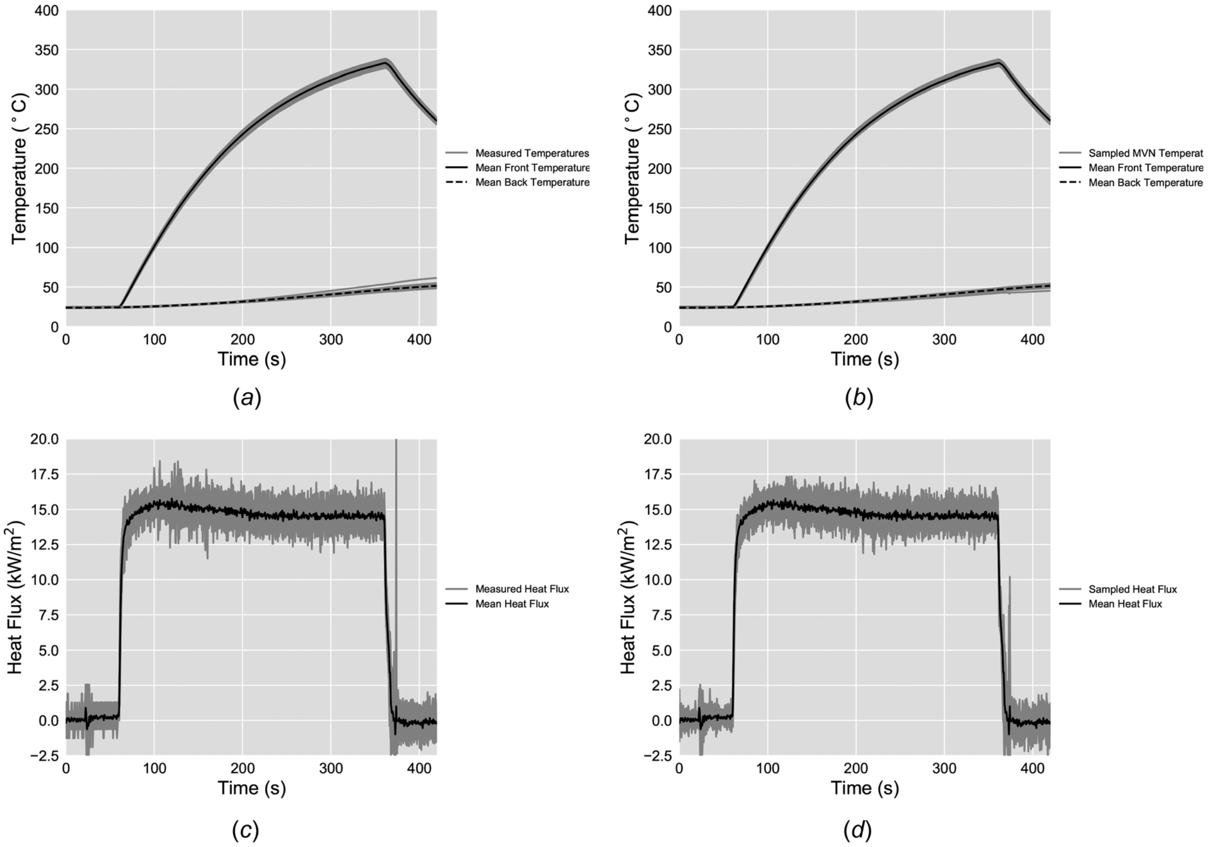

(*a*) (*b*)

(*c*) (*d*)

Fig. 3 Measured temperatures from 20 DFTs subjected to 15 kW/m^2 (*a*). Sampled temperatures from multivariate normal distributions given by Eq. (28) for 15 kW/m^2 (*b*). The solid and dashed lines represent the sample means for each case for the front and back temperatures, respectively. The gray lines indicate individual test runs for the 20 DFTs or samples from the multivariate normal distributions. (*c*) and (*d*) show the measured and sampled temperatures evaluated using the 1D conduction model. Gray lines represent 20 individual measured or sampled temperatures evaluated using the model. Solid black lines represent the mean temperatures evaluated using the model.

resultant likelihood for the set of I independent observations for L testing campaigns is then

$$P\left(D|\theta,\sigma^2_{\mathrm{DFT},A}\right) = \left(\frac{1}{2\pi\sigma^2_{\mathrm{DFT},A}}\right)^{IL/2} \exp\left[-\frac{1}{2\sigma^2_{\mathrm{DFT},A}}\sum_{il}\left(\bar{q}_{il}^{(\mathrm{inc},r)} - \hat{\bar{q}}_{il}^{(\mathrm{inc},r)}\right)^2\right] \tag{31}$$

The maximum likelihood estimator for the parameters of interest is then defined as

$$\hat{\theta} = \arg\max_{\theta\in\mathbb{R}^2}\{P(D|\theta,\sigma^2_{\mathrm{DFT},A})\} \tag{32}$$

The maximum likelihood estimators for $\hat{C}$ and $\hat{\varepsilon}$ cannot be found analytically because of the nature of the 1D conduction model. Instead, the parameters are found using Nelder–Mead optimization via the SciPy optimization function in the programming language Python [25].

5.2.2 Bayesian Parameter Calibration. The statistical model used for the Bayesian case is similar to that presented for the maximum likelihood estimate, Eq. (30). The important difference is that temperatures sampled from the multivariate normal distribution, Eq. (28), is used as model predictors instead of just the mean temperatures

$$\bar{q}_{il}^{(\mathrm{inc},r)} = \hat{q}_{ikl}^{(\mathrm{inc},r)} + e_q; \quad e_q \sim N(0,\sigma^2_{\mathrm{DFT},A}) \tag{33}$$

where $\hat{q}_{ikl}^{(\mathrm{inc},r)}$ is the predicted heat flux for front and back temperatures, $T_{kl,f}$, $T_{kl,b}$ given the parameters of interest θ. The modeling error term is represented by $\sigma^2_{\mathrm{DFT},A}$. The full likelihood is then represented by

$$P\left(D|\theta,\sigma^2_{\mathrm{DFT},A}\right) = \left(\frac{1}{2\pi\sigma^2_{\mathrm{DFT},A}}\right)^{\mathrm{IKL}/2} \exp\left[-\frac{1}{2\sigma^2_{\mathrm{DFT},A}}\sum_{ikl}\left(\bar{q}_{il}^{(\mathrm{inc},r)} - \hat{q}_{ikl}^{(\mathrm{inc},r)}\right)^2\right] \tag{34}$$

where the triple product/sum has been omitted for brevity. The conditional distribution for our parameters of interest given Bayes' rule is then

$$P(\theta|D,\sigma^2_{\mathrm{DFT},A}) \propto P(\theta)P(D|\theta,\sigma^2_{\mathrm{DFT},A}) \tag{35}$$

The conditional distribution for the modeling uncertainty term is

$$P(\sigma^2_{\mathrm{DFT},A}|D,\theta) \propto P(\sigma^2_{\mathrm{DFT},A})P(D|\theta,\sigma^2_{\mathrm{DFT},A}) \tag{36}$$

An informative prior distribution was defined for the emissivity of the DFTs using measurements taken using the FLIR E40 IR camera [10]. A mean and standard deviation for the emissivity were measured to be 0.95 and 0.01, respectively. These values were moment matched to the parameters defining a Beta distribution whose support is $\varepsilon \in [0,1]$

Table 3 Posterior means for C, ε, and $\sigma^2_{\mathrm{DFT},A}$

Parameter	Posterior mean	95% HPD region
C	0.650	0.642–0.659
ϵ	0.938	0.936–0.941
$\sigma^2_{\mathrm{DFT},A}$ (kW/m^2)	0.995	0.983–1.007

$$\alpha = \left(\frac{1-\mu}{\sigma^2} - \frac{1}{\mu}\right)\mu^2; \quad \beta = \alpha\left(\frac{1}{\mu} - 1\right) \tag{37}$$

A vague uniform prior was used for C and a vague half normal prior was used for the modeling uncertainty term

$$\varepsilon \sim \mathrm{Beta}(450.3, 23.7) \tag{38}$$

$$C \sim U(0,1) \tag{39}$$

$$\sigma^2_{\mathrm{DFT},A} \sim \mathrm{HalfNorm}(0,100) \tag{40}$$

Again, given the nature of the 1D conduction model, an analytical, closed form for the posterior distributions cannot be defined. A metropolis random walk, MCMC algorithm was implemented using PyMC3 to sample posterior distributions given the priors in Eq. (38) and the likelihood in Eq. (34). The chains for C and ε were instantiated at their maximum likelihood estimate, $\hat{C}$ and $\hat{\varepsilon}$. The other chains were instantiated at their respective means. Tuning of variance in the proposal distributions was carried out such that the acceptance ratio approaches between 0.234 and 0.45 [26]. An optimal acceptance ratio of 0.45 pertains to one-dimensional problems with the optimal acceptance ratio asymptotically approaching 0.234 for higher dimensional problems. Tuning samples were discarded and the subsequent samples were used to inform the posterior distributions. Results of the calibration process are presented in Sec. 6.

6 Results

6.1 Parameter Calibration. The maximum likelihood estimators for $\hat{C}$ and $\hat{\varepsilon}$ found using Nelder–Mead had values of 0.63 and 0.93, respectively. A summary of the statistics for the posterior distributions and traces for the priors outlined in Eq. (38) are presented in Table 3.

The maximum likelihood estimate and posterior mean for C agree well with each other, but a typical value of C of 0.54 can be found in Frank et al. for natural convection on the surface of a hot plate [11].

Model predictions at the maximum likelihood estimators, and posterior means for the Bayesian parameter calibration are shown in Fig. 4(*a*) using mean temperatures along with the SB gauge response at 15 kW/m^2 (the 5 kW/m^2 and 10 kW/m^2 results have been omitted for brevity). The results of the calibration process show good agreement for both the maximum likelihood estimator and the posterior means.

An estimate for the total uncertainty given the uncertainty from the SB gauge and the modeling uncertainty is given by

$$\sigma^2_{\mathrm{DFT,tot}} = \sigma^2_{\mathrm{DFT},A} + \sigma^2_{\mathrm{sb,tot}} \tag{41}$$

where $\sigma^2_{\mathrm{sb,tot}}$ is from Eq. (23) and represents the total uncertainty from the SB gauge. Figure 4(*b*) shows model predictions given the posterior means along with the 95% Bayesian credible region. The uncertainty presented is dominated by the modeling uncertainty term which accounts for about 82% of the total uncertainty at an incident heat flux of 15 kW/m^2. 16.8% of the total uncertainty is attributed to the type B uncertainty reported by the manufacturer for the SB gauge, and the remainder is attributed by the type A uncertainty of the SB gauge. This translates to about a 7% uncertainty on the measurement for the DFT at an incident heat flux of 15 kW/m^2. Note that because the influence of the calibration uncertainty reported by the manufacturer diminishes at lower heat fluxes, the overall uncertainty becomes more and more dominated by the modeling uncertainty term. At 5 kW/m^2 the uncertainty on the measurement for the DFT is about 20%. The total uncertainty as a function of incident heat flux can be summarized by

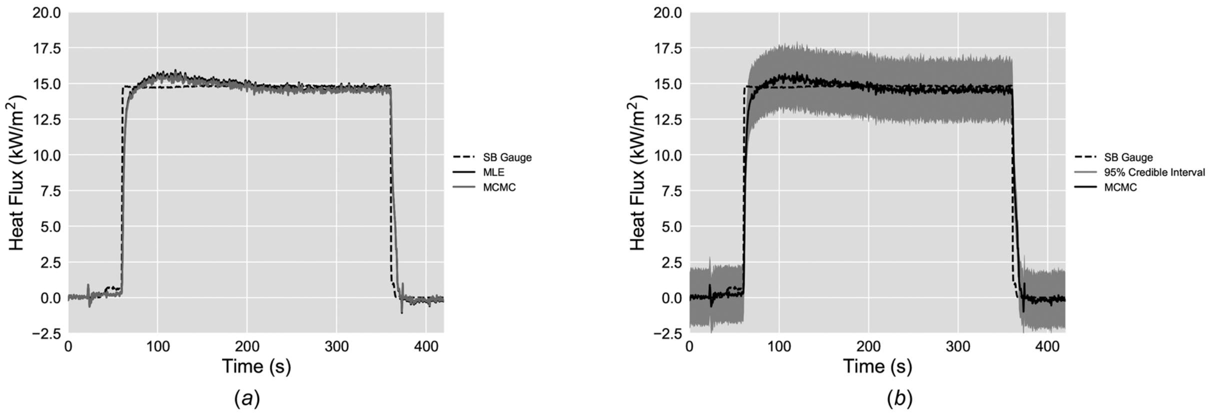

(*a*) (*b*)

Fig. 4 Predictions of heat fluxes from the calibrated models at 15 kW/m^2. The dashed lines, the solid black, and the solid gray lines represent the mean heat flux measured by the SB gauge, the model predictions using the MLE, and the mean model prediction using MCMC, respectively (*a*). In (*b*) the dashed lines represent the heat fluxes measured using the SB gauge, the solid black line represents the predicted fluxes from the mean of the posterior values, and the gray lines represent the 95% Bayesian credible interval.

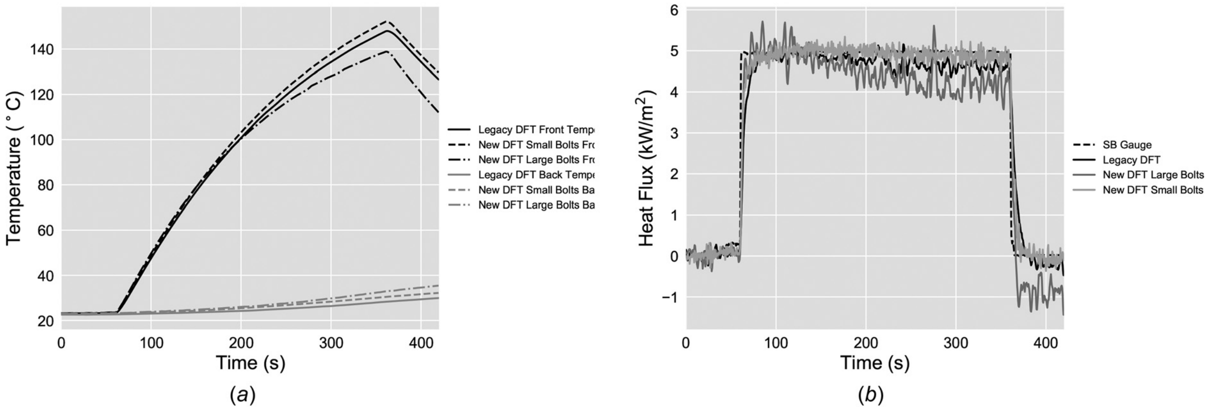

(*a*) (*b*)

Fig. 5 Comparison of the temperatures (*a*) and predicted heat fluxes (*b*) between the typical, legacy DFT, the modified DFT with legacy fasteners, and the modified DFT with new fasteners, at 5 kW/m^2. The black lines represent the front temperatures and gray lines represent the back temperatures in (*a*). The solid lines are for the legacy DFT, the dashed–dotted lines represent the modified DFT with legacy fasteners, and the dashed lines represent the modified DFT with new fasteners. The dashed line in (*b*) represents the SB gauge measured flux and the black, dark gray, and light gray lines represent the predicted flux at 5 kW/m^2 for the legacy and modified DFTs, respectively, using the 1D conduction model.

$$\sigma_{\mathrm{DFT,tot}} = \sqrt{(0.12)^2 + (0.03 \cdot q_{\mathrm{inc}})^2 + (0.995)^2} \qquad (42)$$

A comparison of the modified DFT with legacy fasteners, the modified DFT with smaller fasteners, and the legacy (i.e., typical) DFT evaluated using the 1D conduction model is shown in Fig. 5 at 5 kW/m^2. As was stated earlier, use of the legacy fasteners with the smaller DFT plates resulted in significant conduction losses through the fasteners as can be seen by the lower temperature of the front plate in Fig. 5(*a*) (the dashed-dot red line). The result is a significant under-prediction of the heat flux at later times illustrated by the dark gray line in Fig. 5(*b*). The temperatures and predictions of the modified DFT with smaller fasteners show good agreement with the typical DFT adding weight to the design considerations for the modified DFT.

6.2 Model Components. Components of the predicted incident heat flux evaluated at the posterior means given by Eq. (6) are shown in Fig. 6 along with the SB gauge response at 15 kW/m^2. The figure shows the total incident heat flux, $q_{\mathrm{inc},r}$, the broken down energy components stored in the DFT, as well as the radiation and convective components; $q_{\mathrm{rad}}/\varepsilon$ and $q_{\mathrm{conv}}/\varepsilon$, respectively.

6.3 Model Comparison. The 1D conduction model evaluated at the posterior means is compared to the ESM and it performs better than the ESM model for the three cases tested with the 15 kW/m^2 case presented in Fig. 7. The root-mean-squared error for the model predictions is shown in Table 4 and is defined as $\mathrm{RMSE}_l = \sqrt{\left((1/I)\sum_{i=1}^{I}(\bar{q}_{il} - \hat{q}_{il})^2\right)}$ where $\hat{q}_{il}$ is the prediction with either the 1D conduction model or the ESM and $\bar{q}_{il}$ is SB gauge measurement.

The RMSE for the 1D conduction model is 70% smaller than the RMSE for the ESM for all three cases presented. The ESM performs poorly because of the approximations made to the energy storage and the conduction in the insulation material (see Eq. (12)).

7 Conclusions

This work has shown the implementation of a modified DFT as well as the introduction of a new thermal model for predicting the incident heat flux to the device. Calibration of the DFT in a controlled environment using the radiant element from an ASTM E1354 cone calorimeter with measurements made by an SB gauge as the ground truth was also presented.

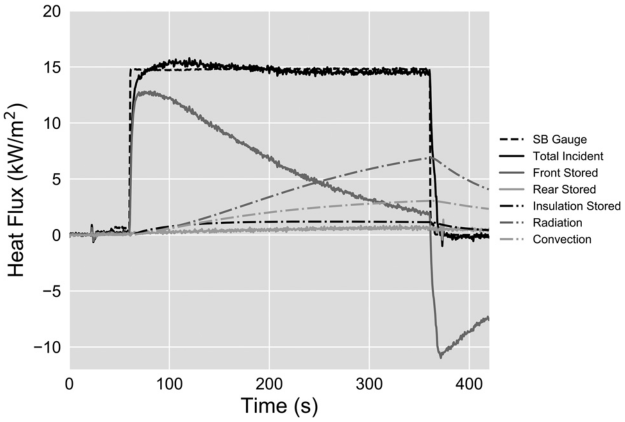

Fig. 6 Components of the heat transfer mechanisms given the calibrated model at 15 kW/m^2. The dashed black line represents measurements from the SB gauge, the solid black line represents the total incident radiation, $q_{\mathrm{inc},r}$, the solid dark gray line represents the energy stored in the front plate, $q_{\mathrm{st},f}$, the solid light gray line represents the energy stored in the back plate, $q_{\mathrm{st},b}$, the dash-dotted black line represents the energy stored in the insulation, $q_{\mathrm{st,ins}}$, the dash-dotted dark gray line represents the radiative losses, q_{emit}, and the dash-dotted light gray line represents the convective losses, q_{conv}.

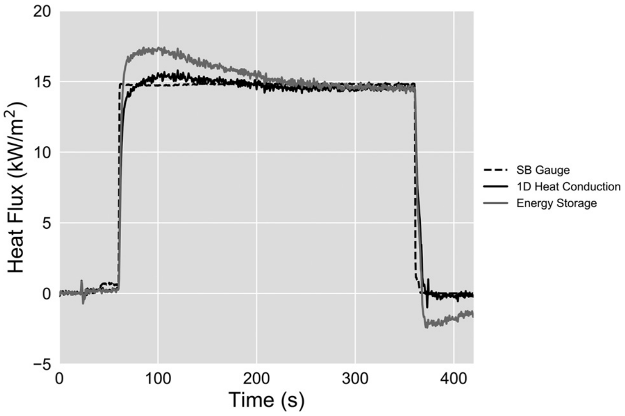

Fig. 7 A comparison of the 1D conduction model versus the ESM model at 15 kW/m^2. The dashed lines represent measurements from the SB gauge, the black line represents predicted heat fluxes from the 1D conduction model, and the gray line represents predicted heat fluxes using the ESM.

A Bayesian statistical framework was used throughout to infer parameters of interest and quantify uncertainties. Uncertainty quantification of the SB Gauge showed that type A uncertainties of 0.12 kW/m^2 would dominate at lower heat fluxes, whereas, the type B uncertainty of ±3% of the measured value begins to dominate the uncertainty in heat flux measurements at higher incident heat fluxes. A methodology was introduced to smooth noise generated during the acquisition of DFT temperatures in the data collection process by approximating the data generation process by multivariate normal distributions with parameters inferred from the data.

The maximum likelihood estimate and Bayesian parameter calibration framework were presented for calibrating C and ε of the 1D conduction model. The maximum likelihood estimator and the Bayesian parameter calibration framework over-predicted C by 18% compared to values in the literature. The Bayesian parameter calibration process also estimated the modeling error to be 0.995 kW/m^2. The relative error, which is a combination of the SB gauge type A uncertainty, the SB gauge type B uncertainty, and the modeling error, was about 20% at an incident heat flux of 5 kW/m^2 and 7% at an incident heat flux of 15 kW/m^2.

Table 4 Root-mean-squared error for the 1D conduction model and the ESM as compared to the SB gauge measurements

Test set	1D conduction RMSE (kW/m^2)	ESM RMSE (kW/m^2)
5 kW/m^2	0.37	0.53
10 kW/m^2	0.77	1.12
15 kW/m^2	1.13	1.66

A comparison between the 1D conduction model and the ASTM E3057 ESM was also presented. The 1D conduction model had root-mean-squared errors between the prediction and SB gauge output of 0.37, 0.77, and 1.13 kW/m^2 for the 5, 10, and 15 kW/m^2 cases, respectively. These values were nearly 70% lower than the ESM whose root-mean-squared errors at 5, 10, and 15 kW/m^2 were 0.53, 1.12, and 1.66 kW/m^2.

In the future it will be necessary to ensure the modeling assumptions presented hold up at higher heat fluxes and longer durations for the 1D conduction model. An interesting analysis would also be performing a scaling analysis on the DFT plate size and fastener diameter to determine the limit of the 1D approximation to conduction through the DFT.

Funding Data

- U.S. National Science Foundation (Award No. 1707090; Funder ID: 10.13039/100000001).

References

[1] James Nakos, T., 2018, "Data Reduction Tools and Uncertainty Analysis of Incident Heat Flux Measurement Tools From Directional Flame Thermometers Used in Hydrocarbon Fuel Pool and Furnace Fires," Sandia National Laboratories, Aberquerque, NM, Report No. SAND2018-10332.
[2] Blanchat, T., Humphries, L. L., and Gill, W., 2002, "Sandia Heat Flux Gauge Thermal Response and Uncertainty Models," *ASTM Special Technical Publication*, 01.
[3] Nakos, J. T., Victor Figueroa, G., and Murphy, J. E., 2005, "Uncertainty Analysis of Heat Flux Measurements Estimated Using a One-Dimensional Heat Conduction Program," Sandia National Laboratories, Aberquerque, NM, Report No. SAND2005-0339.
[4] Blanchat, T. K., and Charles Hanks, R., 2012, "Comparison of the High Temperature Heat Flux Sensor to Traditional Heat Flux Gages Under High Heat Flux Conditions," Sandia National Laboratories, Aberquerque, NM, Report No. SAND2012-10683.
[5] Bryant, R., Johnsson, E., and Ohlemiller, T., 2001, "Estimates of the Uncertainty of Radiative Heat Flux Calculated From Total Heat Flux Measurements," International Conference on Fire Science and Engineering.
[6] Lam, C. S., and Weckman, E. J., 2009, "Steady-State Heat Flux Measurements in Radiative and Mixed Radiative-Convective Environments," Fire Mater., **33**(7), pp. 303–321.
[7] Nakos, J. T., 2005, "Uncertainty Analysis of Steady State Incident Heat Flux Measurements in Hydrocarbon Fuel Fires," Sandia National Laboratories, Aberquerque, NM, Report No. SAND2005-7144.
[8] Erikson, W. W., Nicolette, V. F., Walter, G., and Tieszen, S. R., 2008, "Uncertainty in Propellant Fire Heat Flux—An Experimental and Modeling Approach," Department of Defense Explosives Safety Seminar, Palm Springs, CA, Aug. 12-14, Report No. SAND2008-4487C.
[9] ASTM, 2016, "Standard Test Method for Measuring Heat Flux Using Directional Flame Thermometers With Advanced Data Analysis Techniques," American Society for Testing and Materials, West Conshohocken, PA, Standard No. ASTM E 3057–16.
[10] FLIR, 2020, "User's Manual: FLIR Exx Series," FLIR .
[11] Frank, P. I., David, P. D., Theodore, L. B., and Adrienee, S. L., 2007, *Fundamentals of Heat and Mass Transfer*, 6th ed., Wiley, New York.
[12] Keltner, N. R., Beck, J. V., Nakos, J. T., Parker, A., and Dean, S. W., 2010, "Using Directional Flame Thermometers for Measuring Thermal Exposure," J. ASTM Int., **7**(2), p. 102280.
[13] ASTM, 2007, "Standard Test Method for Heat and Visible Smoke Release Rates for Materials and Products Using an Oxygen Combustion Calorimeter," American Society for Testing and Materials, West Conshohocken, PA, Standard No. ASTM E 1354-04a.
[14] Cox, R. T., 1946, "Probability, Frequency and Reasonable Expectation," Am. J. Phys., **14**(1), pp. 1–13.
[15] Berger, J., 2006, "The Case for Objective Bayesian Analysis," Bayesian Anal., **1**(3), pp. 385–402.
[16] Laplace, P., 1749, *Theorie Analytique Des Probabilites*, Ve. Courcier, Paris, France.
[17] Jeffreys, H., 1945, "An Invariant Form for the Prior Probability in Estimation Problems," Proc. R. Soc., **186**(1007), pp. 453–461.

[18] Jaynes, E. T., 1968, “Prior Probabilities,” IEEE Trans. Syst. Sci. Cybern., **3**, pp. 227–241.

[19] Joint Committee for Guides in Metrology, 2008, “Evaluation of Measurement Data: Guide to the Expression of Uncertainty in Measurement,” .

[20] Gelman, A., Carlin, J., Stein, H., and Rubin, D., 2004, *Bayesian Data Analysis*, 2nd ed., Chapman and Hall/CRC Press, Boca Raton, FL.

[21] D’Agostini, G., 1995, “Probability and Measurement Uncertainty in Physics: A Bayesian Primer,” arXiv preprint hep-ph/9512295.

[22] Rasmussen, C. E., and Williams, C. K. I., 2006, *Gaussian Processes for Machine Learning*, MIT Press, Cambridge, MA.

[23] Dongchu Sun, J. O. B., 2006, “Objective Bayesian Analysis for the Multivariate Normal Model,” ISBA Eighth World Meeting on Bayesian Statistics, Alicante, Spain, June 1-6, pp. 1–38.

[24] Geisser, S., and Cornfield, J., 1963, “Posterior Distributions for Multivariate Normal Parameters,” J. R. Stat. Soc., **25**(2, 5), pp. 368–376.

[25] Gao, F., and Han, L., 2012, “Implementing the Nelder-Mead Simplex Algorithm With Adaptive Parameters,” Comput. Optim. Appl., **51**(1), pp. 259–277.

[26] Roberts, G. O., Gelman, A., and Gilks, W. R., 1997, “Weak Convergence and Optimal Scaling of Random Walk Metropolis Algorithms,” Ann. Appl. Probab., **7**, pp. 110–120.